Chemical Engineering Journal 380 (2020) 122426

Contents lists available at ScienceDirect

Chemical Engineering Journal

journal homepage: www.elsevier.com/locate/cej

Imaging-guided synergistic targeting-promoted photo-chemotherapy against cancers by methotrexate-conjugated hyaluronic acid nanoparticles

Fei Yu[a], Maoshu Zhu[b,f], Nini Li[a], Mingtao Ao[a], Yang Li[e], Mengya Zhong[a], Qian Yuan[a], Huiyu Chen[a], Zhongxiong Fan[e], Yan Wang[a,*], Zhenqing Hou[e,*], Zhongquan Qi[b,*], Yuemao Shen[d,*], Xiao Dong Chen[c,*]

[a] Xiamen Cardiovascular Hospital, Xiamen University, Xiamen 361005, China
[b] Medical College, Guangxi University, Nanning 530004, China
[c] Suzhou Key Lab of Green Chemical Engineering, School of Chemical and Environmental Engineering, College of Chemistry, Chemical Engineering and Materials Science, Soochow University, Suzhou 215123, China
[d] Key Laboratory of Chemical Biology (Ministry of Education), School of Pharmaceutical Sciences, Shandong University, Jinan 250012, China
[e] Department of Biomaterials, College of Materials, Xiamen University, Xiamen 361005, China
[f] Xiang'an Branch, The First Affiliated Hospital of Xiamen University, Xiamen 361101, China

HIGHLIGHTS

- The dual-targeting and reduction-sensitive DOX/ICG@DSHM were developed for chemo-photothermal combination therapy.
- The DOX/ICG@DSHM can achieve on-demand drug release as well as high uptake efficiency.
- The DOX/ICG@DSHM can realize the notable tumor ablation under the guidance of dual-modal optical imaging.

GRAPHICAL ABSTRACT

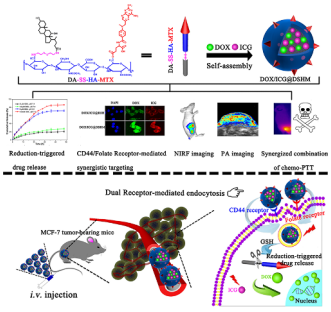

ARTICLE INFO

Keywords:
Tumor-targeted
Indocyanine green
Nanoparticles
Chemo-photothermal combination therapy

ABSTRACT

A combination of chemotherapy and photothermal therapy (PTT) against cancer, overcoming the intrinsic limitations of single-modal chemotherapy or PTT, has emerged as a promising strategy to achieve synergistic therapeutic effect. However, the lack of precise drug delivery and intelligent drug release based on photo-chemotherapy at specific tumor sites remained a challenge. Hence, the both tumor-specific targeting molecule (methotrexate) and ligand (hyaluronic acid)-introduced, glutathione-responsive amphiphiles (deoxycholic acid-hyaluronic acid-methotrexate, DA-SS-HA-MTX) were developed for synchronous delivery of indocyanine green (ICG) and doxorubicin (DOX). The as-synthesized DOX/ICG@DSHM remarkably improved the intracellular drug uptake and accumulation owing to both the CD44/folate receptors-mediated synergistic targeting and the glutathione-triggered rapid drug release. Moreover, DOX/ICG@DSHM efficiently accumulated at the tumor sites, realizing the notable tumor ablation under the guidance of dual-modal optical imaging. Taken together, this study provided a promising nanotheranostic agent for imaging-guided chemo-photothermal combination therapy.

* Corresponding authors.
E-mail addresses: wy@medmail.com.cn (Y. Wang), houzhenqing@xmu.edu.cn (Z. Hou), zqqi@xmu.edu.cn (Z. Qi), yshen@sdu.edu.cn (Y. Shen), xdchen@mail.suda.edu.cn (X.D. Chen).

https://doi.org/10.1016/j.cej.2019.122426
Received 29 April 2019; Received in revised form 18 July 2019; Accepted 4 August 2019
Available online 05 August 2019
1385-8947/

1. Introduction

In recent years, tremendous concerns have been focused on searching for more effective combination therapeutic strategies for cancer [1]. Compared to the conventional chemotherapy, the combined therapeutic strategies possessing many advantages (*e. g.*, simplicity of application and minimally invasive local treatment), which can minimize the side effects and enhance the therapeutic efficiency [2,3]. Among all the various combined treatment approaches, the combination of photothermal therapy and chemotherapy, resulting in superior synergistic effects, has caused the most attentions to optimize cancer therapy. Specially, the indocyanine green (ICG, a unique dye approved by Food and Drug Administration) and doxorubicin hydrochloride (DOX, a clinical approved chemotherapeutic drug) are usually selected in the chemo-photothermal therapy (PTT) [4]. Moreover, it also can utilize the characteristics of the near-infrared (NIR) fluorescence imaging of ICG to realize a real-time monitoring system of cancer theranostics. However, in most of the reported nanosystems [5], the DOX/ICG were just encapsulated into the non-targeted and non-responsive nanoparticles, which cannot avoid the premature release in the blood circulation as well as the insufficient enrichment in the tumor tissues [6,7]. Apparently, it is highly desirable to exploit stimuli responsive nanoscale drug delivery systems for targeted delivery of DOX/ICG.

Because of the defective blood-vessel architectures and the immature lymphatic system which could lead to the enhanced permeability and retention (EPR) effect, nanoparticles are prone to passively accumulate in tumor tissues [8]. However, this passive targeting strategy lacks active targeting ability, which would lead to limited treatment efficacy as well as undesirable drug delivery effects. Therefore, an active targeting strategy, functioning of nanocarrier with receptor targeting ligand, has been actively pursued [9]. Normally, the passive targeting strategy or single targeting strategy still faces severe inherent limitations of their nonspecific uptake by certain kinds of normal cells, which express low or similar levels of receptors as well. It was reported that dual or multiple receptors targeting could overcome this problem by increasing the differentiation between normal and tumor cells [10]. Apparently, to further improve the accumulation of therapeutic drug at tumor sites, two separate tumor-specific ligands could be involved in the same nanoparticles [11]. In this way, dual receptors targeting strategy can deliver nanoparticles to tumor cells effectively and specifically [12].

Among a plethora of targeting ligands, hyaluronic acid (HA) and its

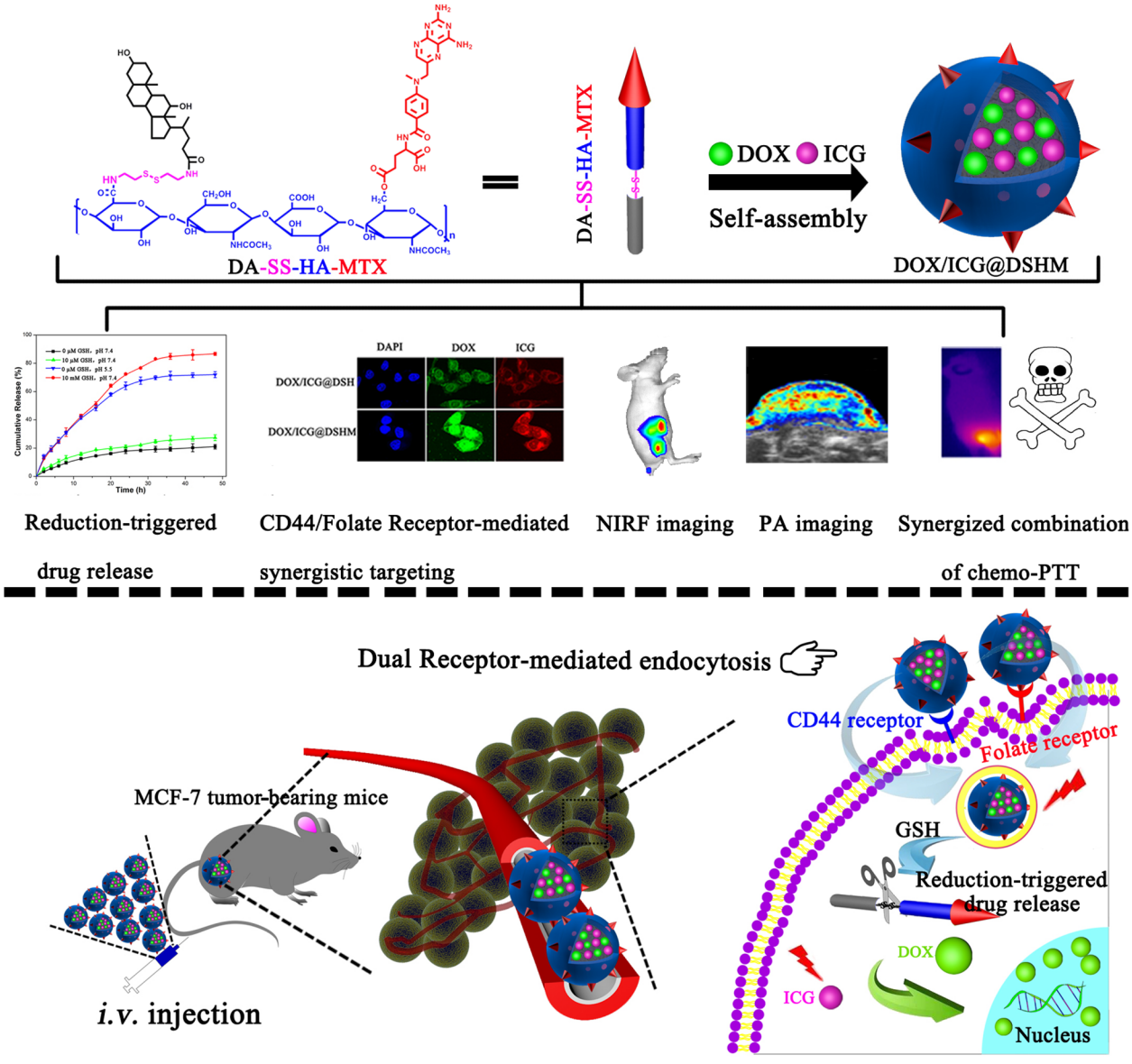

Scheme 1. Schematic diagram of the formation process of DOX/ICG@DSHM with their imaging-guided synergistic targeting-promoted photo-chemotherapy.

derivatives have been extensively investigated in the design of drug carrier in the pharmaceutical fields. Most of HA-based nanoparticles have put emphasis on the over expression of HA binding receptors (*e.g.*, CD_{44}), which has been found over-expressed on the surface of numerous tumor cells. Deservedly, HA-based nanoparticles could exhibit an improved cellular uptake through CD_{44}-mediated endocytosis. Besides, methotrexate (MTX), due to high structural similarity to its analog folic acid (FA), could also be used as a unique 'targeting ligand' with impressive affinity to folate receptors (overexpressed on the surface of a number of different cancer cells) [13–15]. We hypothesized that higher efficient synergistic tumor targeting ability could be achieved by conjugating the nanoparticles with MTX and HA at the same time.

To achieve an ideal therapeutic effect, dealing with fast release of the active payloads at the desired site is another challenge to overcome [16]. Recently, increasing concerns have been focused on the engineering of intracellular stimuli-responsive nanoparticles that are generally stable under nonspecific biodistribution *in vivo* (*e.g.*, in blood circulation) while rapidly release the loaded pharmaceutical agent after entering the target site (*e.g.*, in tumor cells), resulting in markedly improved therapeutic efficacy [17,18]. Notably, redox-responsive nanoparticles, which could be sensitive to differences in the concentrations of glutathione between the intracellular conditions and extracellular environment, are often adopted as the stimulus-responsive nanoscale drug delivery systems [19–21].

In this work, a smart dual-targeting and reduction-sensitive nanosystem was assembled by deoxycholic acid (DA)-hyaluronic acid (HA)-methotrexate amphiphilic copolymer. Firstly, the hydrophobic DA was conjugated with the hydrophilic HA targeting ligand through the disulfide bond (abbreviated as DA-SS-HA). Then, the synthesized DA-SS-HA amphiphilic copolymer was further conjugated with targeting methotrexate molecules (abbreviated as DA-SS-HA-MTX) for dual active targeting. Subsequently, both the DOX and ICG were physically encapsulated within DA-SS-HA-MTX self-assembling nanoparticles (abbreviated as DOX/ICG@DSHM). Meanwhile, both the DOX and ICG were also physically encapsulated within DA-SS-HA self-assembling nanoparticles (abbreviated as DOX/ICG@DSH), which were used as the control. In addition, the insensitive conjugates (abbreviated as DA-CC-HA-MTX) were also synthesized using adipic dihydrazide as the linker. Similarly, the insensitive DOX/ICG loaded nanoparticles (abbreviated as DOX/ICG@DCHM) were also prepared in the same way for comparison.

We hypothesized that once DOX/ICG@DSHM were intravenously administrated, the nanoparticles would preferentially accumulate at the tumor sites via combining of passive targeting of EPR effect-mediated as well as CD_{44}/folate receptors-mediated active targeting mechanisms. After internalization by the tumor cells, the disulfide linkage between HA and DA would induce a rapid drug release of the cargos, achieving an enhanced therapeutic effect. In addition, NIR irradiation would induce local heat generation, which could increase the permeability of cell membranes to effectively enhance the drug uptake. Especially, by utilizing the DOX/ICG@DSHM as the theranostic agent, eradication of tumors would be achieved via the NIR fluorescence imaging-guided chemo-photothermal combination therapy in one treatment cycle (Scheme 1).

2. Result and discussion

2.1. Synthesis and characterization of DA-SS-HA-MTX

The dual-targeting reduction-responsive polymer DA-SS-HA-MTX

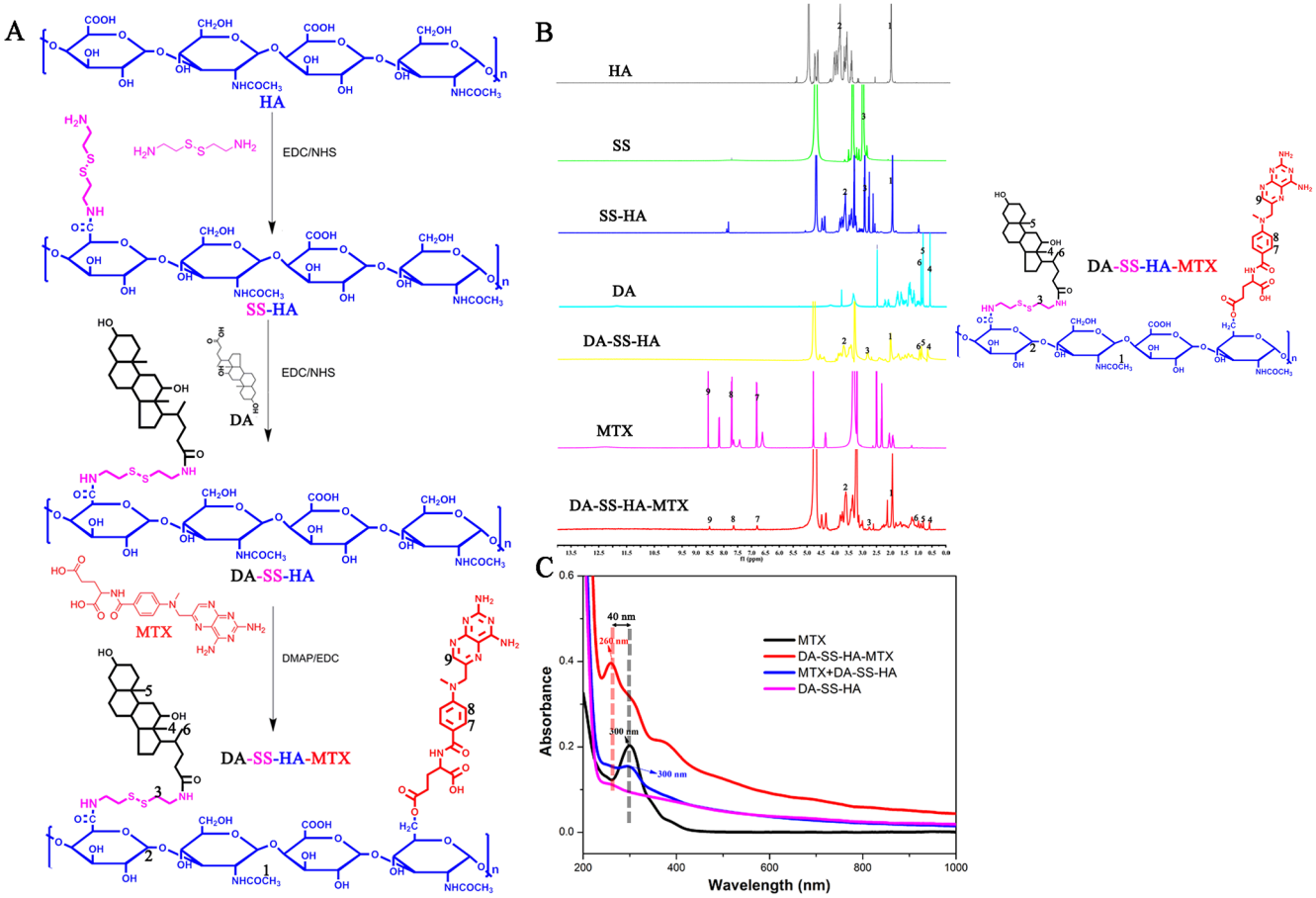

Fig. 1. Characterization of DA-SS-HA-MTX conjugate. (A) Synthetic routes of the DA-SS-HA-MTX. (B) ^{1}H NMR spectra of HA, cystamine, SS-HA, DA, DA-SS-HA, MTX, and DA-SS-HA-MTX. (C) UV–vis spectra of MTX, DA-SS-HA, and DA-SS-HA-MTX.

was synthesized via the three distinctive steps (Fig. 1A). Firstly, cystamine-modified HA (HA-SS) were obtained by coupling the carboxyl group of HA with the amino group of cystamine through carbodiimide-catalyzed amidation reaction. Secondly, HA-cystamine linkers were conjugated to the carboxylic group of DA to obtain DA-SS-HA through amine coupling reaction. Lastly, the γ-carboxylic group of MTX was attached to the hydroxyl group of DA-SS-HA to synthesize DA-SS-HA-MTX through an esterification reaction. The chemical structures of DA-SS-HA-MTX conjugate were further identified by ^{1}H NMR and FT-IR analysis. As shown in Fig. 1B, characteristic peaks of N-acetyl group and hydroxyl groups in HA were found at 1.9 and 4.0 ppm in the spectrum of DA-SS-HA. While the characteristic peaks of methylene groups of cystamine were also appeared at 2.9 ppm in the spectrum of DA-SS-HA. Besides, the successful linkage of DA with HA-SS was confirmed by the characteristic peaks of the methyl group in DA, which appeared at 0.67–1.60 ppm. Furthermore, the successful grafting of MTX on the polymer backbone of DA-SS-HA was indicated by the characteristic peaks at 6.8, 7.7, and 8.6 ppm in the spectrum of DA-SS-HA-MTX, corresponding to the aromatic protons of MTX.

The structure of the DA-SS-HA-MTX was also confirmed by FT-IR analysis (Fig. S1). As compared to the spectrum of DA and HA-SS, the new absorption peaks emerged at 1650 (amide I band) and 1564 cm^{-1} (amide II band) in the spectrum of DA-SS-HA, which were due to the formulation of amide linkage. In the spectrum of DA-SS-HA-MTX, the absorption bands at 1600, 1580, and 1450 cm^{-1} were corresponding to the substituted benzene of MTX, implying the successful linkage of MTX with DA-SS-HA. Moreover, the adsorption peak at 1740 cm^{-1} associated with the newly generated ester bond was also appeared in the spectrum of DA-SS-HA-MTX.

Additionally, the UV–vis spectrum of the DA-SS-HA-MTX was displayed in Fig. 1C. It was observed that the physical mixture of DA-SS-HA and MTX exhibited the superposition of the characteristic peaks of free MTX and DA-SS-HA. Moreover, compared to the characteristic absorption peak of free MTX at 300 nm, there was about a 40 nm blue-shift in the spectrum of DA-SS-HA-MTX at 260 nm. This was possibly caused by the conjugation between MTX and DA-SS-HA. The above results of ^{1}H NMR, FT-IR, and UV–vis analysis confirmed the successful synthesis of DA-SS-HA-MTX, which could be further used as an important self-assembly motif to construct the dual receptor-targeted redox-responsive drug delivery systems. In addition, as a control group, the structure of synthesized insensitive amphiphilic polymer DA-CC-HA-MTX (Fig. S2) was also identified by ^{1}H NMR analysis (Fig. S3).

2.2. Preparation and characterization of DOX/ICG@DSH and DOX/ICG@DSHM

Because of the amphiphilicity, DA-SS-HA or DA-SS-HA-MTX conjugate could be readily self-assembled into nanoscale structure in aqueous solution using dialysis method to encapsulate chemotherapeutic drug (DOX) and photothermal drug (ICG) (designed as DOX/

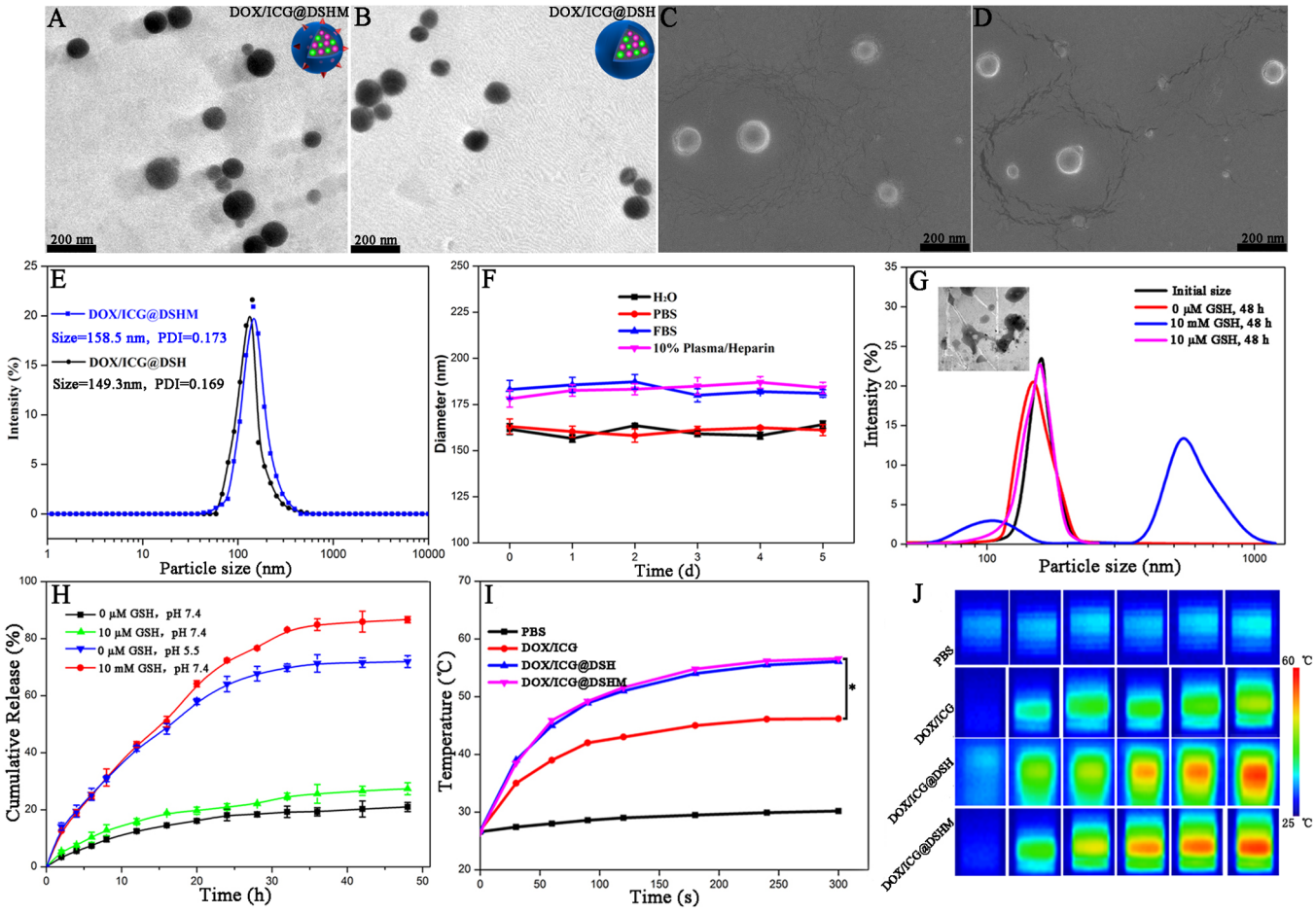

Fig. 2. TEM image of (A) DOX/ICG@DSHM and (B) DOX/ICG@DSH. SEM image of (C) DOX/ICG@DSHM and (D) DOX/ICG@DSH. (E) Hydrodynamic diameter of DOX/ICG@DSHM and DOX/ICG@DSH. (F) Size stability of DOX/ICG@DSHM nanoparticles in DI water, PBS, 10% plasma/Heparin in PBS, and FBS within 5 d. (G) Size changes of DOX/ICG@DSHM after incubation in PBS containing 0 μM, 10 μM, or 10 mM of GSH. Inset: Morphological change of DOX/ICG@DSHM detected by TEM after incubation with GSH for 48 h. (H) Drug release of DOX from DOX/ICG@DSHM after incubation under different conditions. (I) Temperature profiles of PBS, DOX/ICG, DOX/ICG@DSH, and DOX/ICG@DSHM under the continuous laser irradiation at a power intensity of 1 W/cm^2. (J) Infrared thermographic images of PBS, DOX/ICG, DOX/ICG@DSH, and DOX/ICG@DSHM were recorded for 5 min with an infrared thermal imaging camera after continuous laser irradiation.

ICG@DSH or DOX/ICG@DSHM) [22]. The hydrodynamic particle size, surface charge, and particle size distribution of the DOX/ICG@DSH and DOX/ICG@DSHM were measured by dynamic light scattering. The hydrodynamic particle size of the DOX/ICG@DSH and DOX/ICG@DSHM were about 149.3 nm and 158.5 nm with low polydispersity index (≤ 0.20), indicating a narrow size distribution of these two kinds of nanosystems (Fig. 2E). The morphology of the DOX/ICG@DSH and DOX/ICG@DSHM was also observed by transmission electron microscopy (TEM) (Fig. 2A and B) and scanning electron microscope (Fig. 2C and D), indicating that these two kinds of nanosystems exhibited spherical shape, excellent monodispersity, and uniform size distribution. The zeta potential of DOX/ICG@DSHM was about −33.5 mV, which was due to the presence of deprotonated carboxylic groups on the surface of nanosystems. Moreover, the negatively charged nanoparticles could enhance their circulation half-life, which was ascribed to their less adsorption to plasma protein [8]. Drug encapsulation efficiency (EE) and drug-loading efficiency (LE) were important for further clinical application of nanosystems. Herein, the EE of DOX and ICG of DOX/ICG@DSHM was measured as about 90.5% and 85.9%, respectively. And, the LE of DOX and ICG of DOX/ICG@DSHM was measured as approximately 7.7% and 7.3%. Meanwhile, the EE of DOX and ICG of DOX/ICG@DSH was measured as about 89.6% and 83.2%, respectively. Besides, the LE of DOX and ICG of DOX/ICG@DSH was measured as approximately 7.6% and 7.1%.

2.3. Stability and photothermal efficiency of DOX/ICG@DSHM

The size stability of DOX/ICG@DSHM were assayed in deionized (DI) water, phosphate buffered saline (PBS), fetal bovine serum (FBS), and 10% (v/v) plasma/heparin in PBS respectively (Fig. 2F). The DOX/ICG@DSHM in DI water and PBS remained similarly to initial size, implying an excellent long-term stability of nanosystems against ionic effect. In addition, the stability was also observed by dispersing the DOX/ICG@DSHM in FBS or plasma/heparin solution. As shown in Fig. 2F, the initial size of DOX/ICG@DSHM remained unchanged basically, indicating that the protein binding has few effects on the stability. These results confirmed that the DOX/ICG@DSHM possessed excellent size stability in different complex physiological environment.

ICG is an FDA-approved agent to be applied in visual diagnostic and photothermal therapy. Unfortunately, the further application of ICG is limited by its numerous drawbacks (*i.e.* instability in aqueous solution and prone to self-bleaching) [9]. Thus, the fluorescence stability of ICG@DSHM was measured by fluorescence analysis (Fig. S4). After 5 days, the fluorescence intensity of ICG@DSHM remained nearly ~90.1%, whereas the fluorescence intensity of free ICG decreased to ~50% of initial intensity. These results indicated that the fluorescence stability was effectively enhanced by encapsulating ICG into ICG@DSHM. The protective effect of ICG@DSHM might be ascribed to the encapsulation of ICG into the nanoparticles, which isolated it from the aqueous solutions.

In order to observe the photothermal efficiency of DOX/ICG@DSHM, we investigated the temperature increasing profiles under laser irradiation (808 nm, 1 W/cm^2) using an infrared thermal imaging camera (Fig. 2I and J). Under the laser irradiation (808 nm, 1 W/cm^2) for 5 min, the temperature of PBS, free ICG, DOX/ICG@DSH, and DOX/ICG@DSHM increased to 29.1, 42.3, 53.9, and 54.3 °C respectively. DOX/ICG@DSH and DOX/ICG@DSHM displayed a higher temperature increase than that of free ICG under laser irradiation, which may be due to the enhancement of ICG stability by encapsulating it into the nanoparticles.

2.4. Redox-induced destabilization of DOX/ICG@DSHM

In order to investigate the reduction responsiveness, the DOX/ICG@DSHM were incubated with different concentrations of GSH solutions, which mimicked the distinctive environments *in vivo*. The respective variations of morphologies and hydrodynamic particle sizes of the DOX/ICG@DSHM were monitored. As shown in Fig. 2G, the hydrodynamic particle size of the DOX/ICG@DSHM increased to 529.7 nm after being exposure to 10 mM of GSH (corresponding to the levels in tumor cells) for 48 h, accompanying with broadening of size distribution. This might be attributed to the cleavage of the disulfide linkages between the HA polymer and DA molecules, which lead to the disassembly of the nanoparticles followed by the formation of aggregation/precipitation. These results were also confirmed by the typical TEM images of DOX/ICG@DSHM after incubation with 10 mM of GSH for 48 h (Fig. 2G). In contrast, when immersed the DOX/ICG@DSHM into 0 mM or 10 μM of GSH (mimicking the plasma levels), no obvious variation in morphology and hydrodynamic particle size was observed after 48 h, indicating that the DOX/ICG@DSHM could keep stable in the blood circulation.

2.5. In vitro reduction-responsive release

Drug delivery systems, which could be capable of fast releasing pharmaceutical agent at desired site, are tending to induce enhanced therapeutic effect [23]. In order to assess the reduction-responsive release behavior of DOX/ICG@DSHM, the *in vitro* cumulative release of DOX was conducted in presence of different GSH/pH levels. The cumulative DOX release profiles were displayed in Fig. 2H. Firstly, both the DOX/ICG@DSHM and DOX/ICG@DCHM displayed pH-dependent drug release behavior with greater rate of drug release at lower pH value. Besides, in the absence of GSH (pH = 7.4), the DOX/ICG@DSHM exhibited an initial fast drug release with ~15% of DOX released within 12 h. However, little drug release was observed during the following 18 h and approximately ~28% of cumulative drug release was obtained at 48 h. This insufficient DOX release could be ascribed to the encapsulation of DOX within the hydrophobic core of nanoparticles. In addition, in the presence of 10 μM of GSH (mimicking the plasmatic levels), the release profile displayed the similar pattern, in which ~18% of DOX was released at initial 12 h, followed by slow release in the subsequent 36 h. In contrast, in the presence of 10 mM of GSH (mimicking tumor cells environment), the drug release rate was dramatically accelerated, in which ~38% of DOX was released within 12 h and almost attained over ~85% at 48 h. This accelerated release of DOX from DOX/ICG@DSHM might be attributed to the rapid cleavage of disulfide bonds, which would result in the disassembly of nanosystems associated with the destruction of structural integrity of the nanoparticles, and thus promote the diffusion of drug from the hydrophobic core of nanoparticles. In addition, only ~21% of DOX released from DOX/ICG@DCHM in the presence of 10 mM of GSH at 48 h (Fig. S5).

The results above indicated that the DOX/ICG@DSHM would be stable in the plasma after intravenous administration without releasing a substantial amount of DOX, whereas could trigger the drug release inside tumor cells with a rapid pattern. Therefore, the DOX/ICG@DSHM are expected to be a kind of highly promising drug delivery system to control the release of anticancer drug smartly for improvement of therapeutic efficacy.

2.6. Cellular uptake study

The cellular uptake study of the DOX/ICG@DSHM was visualized by the confocal laser scanning microscopy (CLSM). MCF-7 cells, highly expressed folate and CD_{44} receptor on the surface of cell membrane, were incubated with DOX/ICG@DSHM for 1 and 4 h. The cellular uptake of DOX/ICG and DOX/ICG@DSH was performed for comparison. As shown in Fig. 3, the fluorescence signal of DOX was primarily existed in the nuclei of MCF-7 cells in the free DOX solution-treated group, which was attributed to the fact that small DOX molecules entered MCF-7 cells through passive diffusion. Conversely, the fluorescence signal of DOX in MCF-7cells treated with DOX/ICG@DSHM seemed to be existed in the cytoplasm as well as nuclei, indicating DOX/ICG@

DSHM were taken up into MCF-7 cells by endocytosis. Besides, the fluorescence signal of ICG was homogenously distributed in the cytoplasm in MCF-7 cells in the free ICG solution-treated group, which was attributed to the binding interaction of ICG with intracellular protein (glutathione S-transferase) [24]. Specially, the free doxorubicin hydrochloride was taken up rapidly by MCF-7 cells, principally owing to the fast passive diffusion of small molecule across cellular membranes [25,26]. On the contrary, due to altered uptake pathway, the fluorescence intensity of DOX and ICG in MCF-7 cells treated with DOX/ICG@DSHM gradually increased with the incubation of time, indicating classical time-dependent cellular uptake behavior.

In addition, the stronger fluorescence signal of both DOX and ICG was observed in the DOX/ICG@DSHM-treated groups. This finding indicated that the simultaneous decoration of both MTX and HA on the surface of the nanoparticles would enhance the cellular uptake. Especially, it should be worth noting that the green fluorescence signal of DOX could be detected in the cell nuclei of MCF-7 cells after 4 h incubation with the DOX/ICG@DSHM, indicating the efficient cellular uptake of DOX/ICG@DSHM and subsequent desired intracellular release of DOX.

To investigate the dual receptor-targeting mechanism of DOX/ICG@DSHM, the competitive experiments by pre-treating with excess free FA/HA were conducted. As shown in Fig. 4A, the fluorescence signal of the DOX/ICG@DSHM groups was apparently weakened when the free HA or free FA were pre-incubated in the cell culture medium. This was due to the significant decrease of availability of both folate and CD_{44} receptors on the surface of MCF-7 cells. This result demonstrated that DOX/ICG@DSHM could specifically interact with folate and CD_{44} dual receptors. This targeted drug delivery strategy would lead to enhanced therapeutic efficiency as well as reduction of side effects.

The cellular uptake efficiency of DOX/ICG@DSHM-treated cancer cells with or without pre-incubation of folate and HA was also quantitatively determined by flow cytometry. As shown in Fig. 4B, the values of the fluorescence intensity of DOX/ICG@DSHM increased as compared to that of the DOX/ICG@DSH, which was attributed to the synergistic enhancement of drug uptake efficiency via dual receptor-mediated endocytosis. Meanwhile, pre-treating with excess amount of FA or HA in the DOX/ICG@DSHM-treated MCF-7 cells could significantly reduce the fluorescence intensity in comparison to the DOX/ICG@DSHM group without pre-treatment. Thus, both qualitative and quantitative results confirmed that the DOX/ICG@DSHM could bind to both folate and CD_{44} receptors specifically and selectively, resulting in the synergistic targeting effect.

To further test the dual receptor-targeting mechanism of DOX/ICG@DSHM, we measured the targeting specificity of DOX/ICG@DSHM using MCF-7 cells with high-level folate/CD44 receptor expression, A549 cells with high-level CD44 receptor expression and the normal LO2 cells with low-level folate/CD44 receptor expression.

Flow cytometry was used to quantify the cellular uptake of DOX/ICG@DSHM by these three kinds of cells (Fig. S7). The fluorescence intensity from DOX/ICG@DSHM in MCF-7 cells was stronger than that of A549 cells, indicating that fewer DOX/ICG@DSHM were uptaken by A549 cells. This was ascribed to low-level expression of folate receptor on the surface of the A549 cells. Meanwhile, the LO2 cells displayed the weakest fluorescence intensity, indicating that fewest DOX/ICG@DSHM were taken into normal cells. This was attributed to extremely low-level expression of both folate and CD44 receptors on the surface of the LO2 cells.

Specially, the fluorescence intensity from DOX/ICG@DSHM in MCF-7 cells was approximately 2.1 and 3.8-fold higher than that in

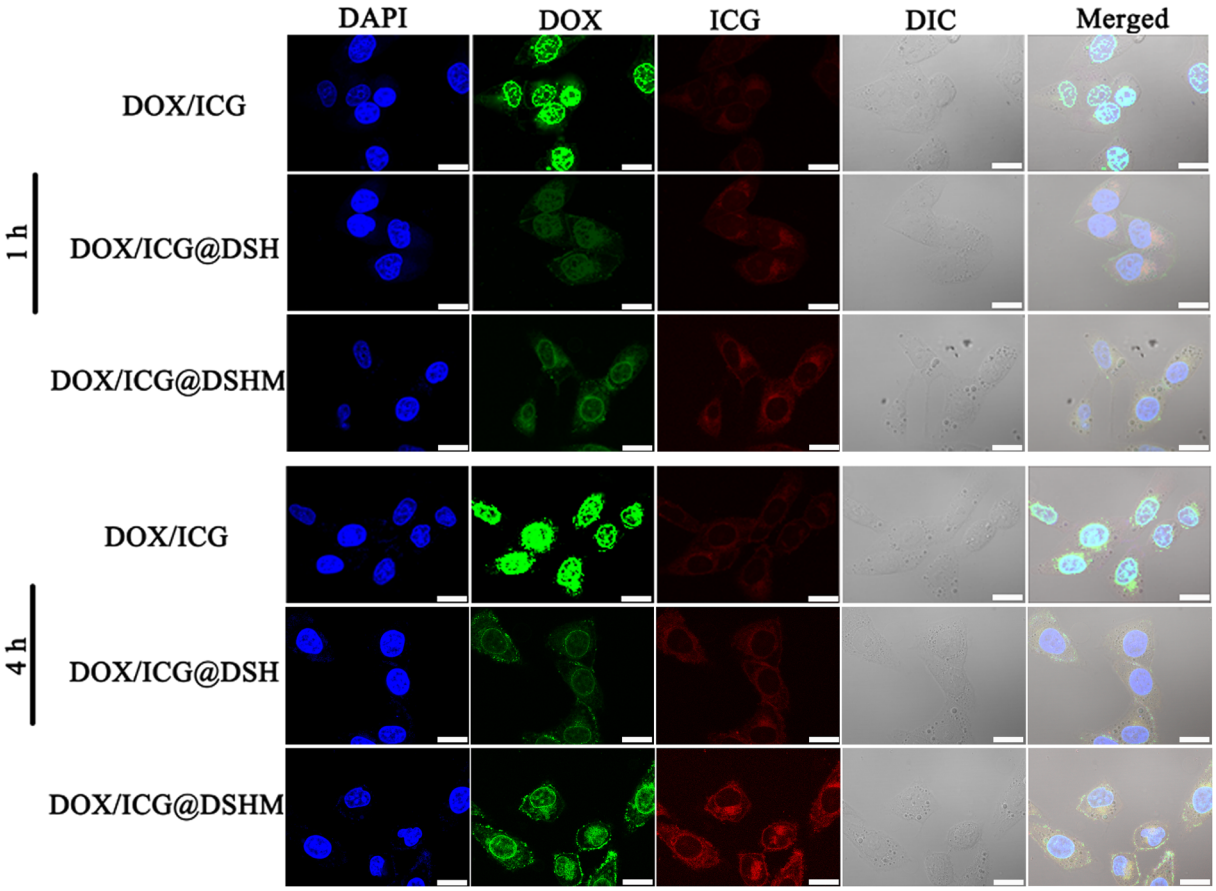

Fig. 3. Confocal laser scanning microscopy images of MCF-7 cells incubated with DOX/ICG, DOX/ICG@DSH, and DOX/ICG@DSHM for 1 and 4 h. Scale bars = 20 μm. Blue signal, DAPI; green signal, DOX; red signal, ICG.

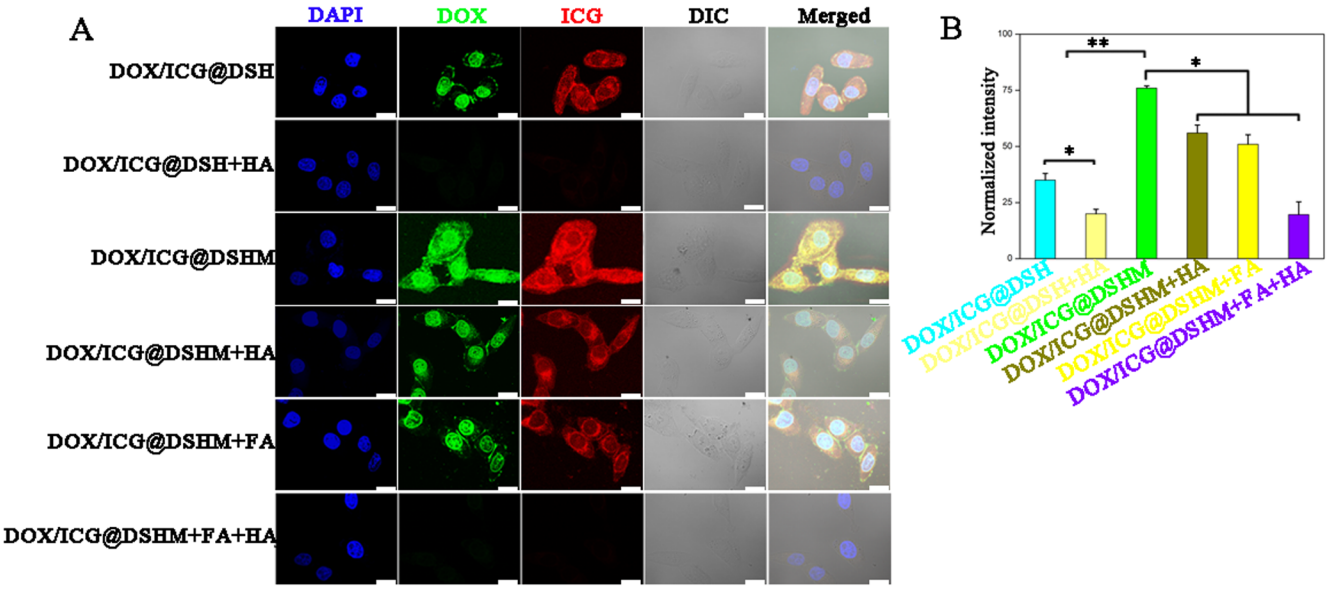

Fig. 4. (A) Confocal laser scanning microscopy of MCF-7 cells incubated with DOX/ICG@DSH and DOX/ICG@DSHM in the absence or presence of free FA/HA after 4 h. Scale bars = 20 μm. (B) Mean fluorescence intensity of MCF-7 cells treated with DOX/ICG@DSH and DOX/ICG@DSHM in the absence or presence of free FA/HA after 4 h.

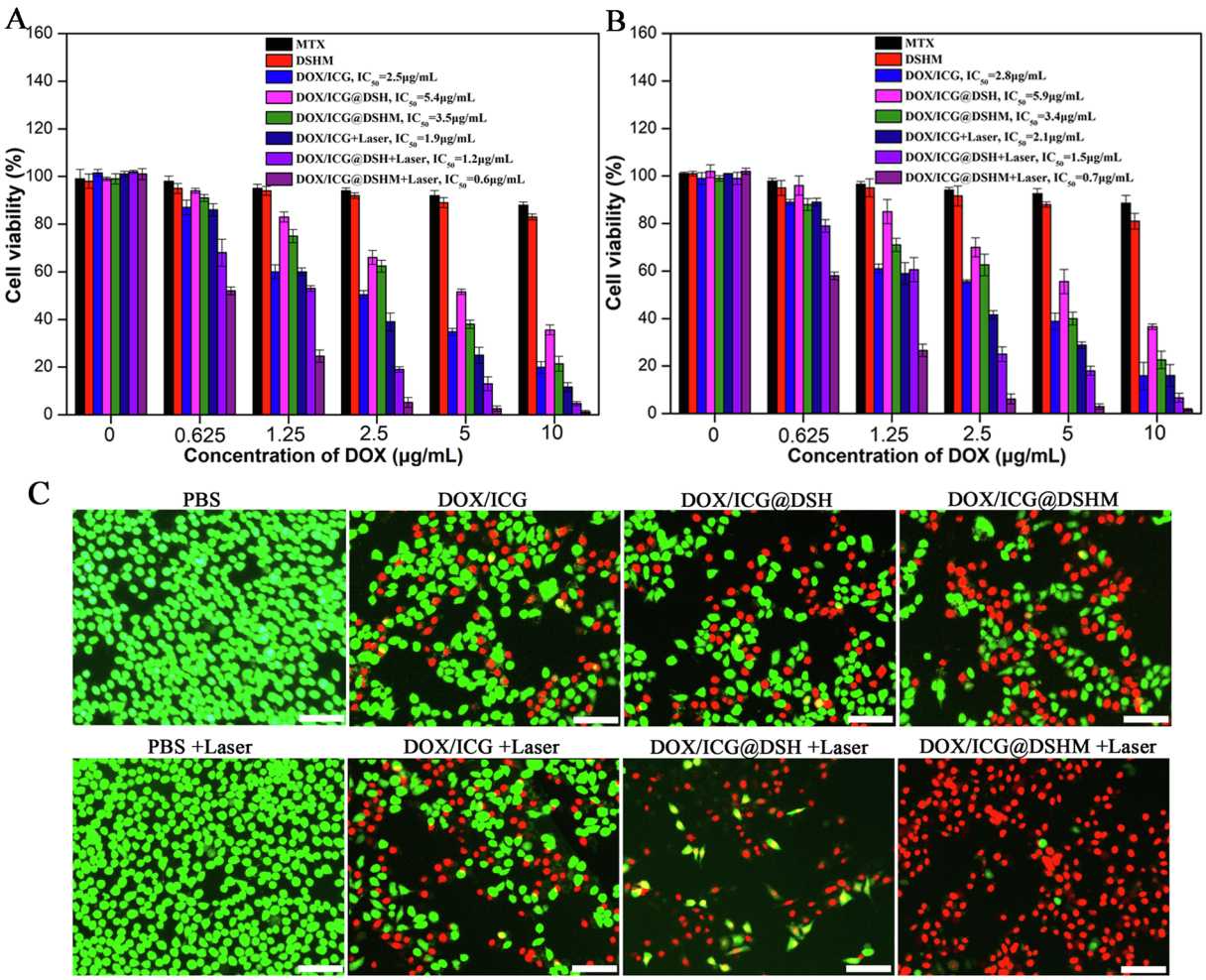

Fig. 5. (A) Cell viability of MCF-7 cells treated with MTX, DSHM, DOX/ICG, DOX/ICG@DSH, and DOX/ICG@DSHM with or without 808-nm laser irradiation (1 W/cm^2, 5 min). (B) Cell viability of Hela cells treated with DOX/ICG, DOX/ICG@DSH, and DOX/ICG@DSHM with or without 808-nm laser irradiation (1 W/cm^2, 5 min). (C) Calcein-AM/PI co-stained fluorescence images of MCF-7 cells treated with PBS, DOX/ICG, DOX/ICG@DSH, and DOX/ICG@DSHM with 808-nm laser irradiation. Living cells were stained green with calcein-AM, and dead cells were stained red with PI. Scale bars = 100 μm.

A549 cells and LO2 cells, respectively. Apparently, DOX/ICG@DSHM NPs possessed highly specific selectivity for folate/CD44 receptors-overexpressed MCF-7 cells.

2.7. Cytotoxicity test

To investigate the chemo-photothermal therapy of the DOX/ICG@DSHM *in vitro*, the viability of MCF-7 cells and HeLa cells bearing single- or dual-modality therapy was assessed by MTT assay. As shown in Fig. 5A and B, in the absence of near-infrared (NIR) laser irradiation, the free DOX, DOX/ICG@DSH, and DOX/ICG@DSHM-treated MCF-7 and HeLa cells displayed an inhibitive effect on the cell proliferation in a dose-dependent manner. Besides, compared with the DOX/ICG@DSH (IC_{50}, 5.4 μg/mL), the DOX/ICG@DSHM (IC_{50}, 3.5 μg/mL) exhibited a significant increase of cytotoxic activity to MCF-7 cells and HeLa cells. This mainly might be the result of the high-efficiency affinity of DOX/ICG@DSHM to these two kinds of cancer cells, which enhanced the uptake of DOX/ICG@DSHM through dual receptor-mediated endocytosis, causing an excellent inhibition of cell proliferation. Besides, this remarkably enhanced cytotoxic activity to MCF-7 cells and HeLa cells could be partly ascribed to the cytotoxicity of MTX.

In the presence of NIR laser irradiation, it was noted that the cell viability of DOX/ICG@DSH (IC_{50}, 1.2 μg/mL) and DOX/ICG@DSHM (IC_{50}, 0.6 μg/mL) groups were much lower than those without irradiation (Fig. 5A). The enhanced cytotoxicity might be attributed to the fact that ICG could induce hyperthermia, which leads to severe photothermal damage on tumor cells. Moreover, the hyperthermia would also trigger the rapid release of DOX from the nanoparticles, which increased the intracellular concentration of DOX and accelerated a faster diffusion of DOX into the nucleus. Lastly, the growth inhibition effect on the cells was promoted.

Subsequently, we further investigated the synergistic cytotoxicity of DOX/ICG@DSHM against MCF-7 cells with chemotherapy from DOX and photothermal injury from ICG. Fig. S8 showed that DOX/ICG@DSHM had the IC_{50} value of 0.6 μg/mL under irradiation, and exhibited significant cytotoxicity advantage over free DOX (IC_{50}, 2.6 μg/mL) and ICG@DSHM under irradiation (IC_{50}, 2.5 μg/mL). Specially, the combination index (CI), providing quantitative information of the combination effect, was also calculated. CI values lower than, equal to, or higher than 1 denote synergism, additivity, or antagonism, respectively. Here, the combination index (CI) was calculated to be 0.5, which indicated the synergistic effect of DOX/ICG@DSHM in photothermal therapy and chemotherapy (CI < 1 represented synergism) [27,28]. Apparently, compared with the monotherapy of photothermal therapy or chemotherapy, the photo-chemotherapy of DOX/ICG@DSHM under irradiation displayed remarkably synergistic therapeutic efficiency.

To visually investigate the *in vitro* therapeutic effect of DOX/ICG, DOX/ICG@DSH, and DOX/ICG@DSHM, MCF-7 cells were stained by calcein-AM and propidium iodide (PI) to distinguish the live and dead cells, respectively. As shown in Fig. 5C, all the MCF-7 cells exhibited green fluorescence in the PBS group, suggesting that the pure laser irradiation is relatively safe. Specially, once laser irradiation was added on the DOX/ICG@DSHM-treated group, great amounts of MCF-7 cells were killed, which was likely caused by hyperthermic cytotoxicity of ICG and chemotherapeutic cytotoxicity of DOX. In addition, hyperthermia could induce the enhancement of membrane permeability, partly augmenting the internalization of DOX. The results suggested that the simultaneous synergistic cytotoxic effect of DOX/ICG@DSHM on MCF-7 cells could be achieved under the laser irradiation. Besides, the above result was in accordance with the MTT assay. Moreover, *in*

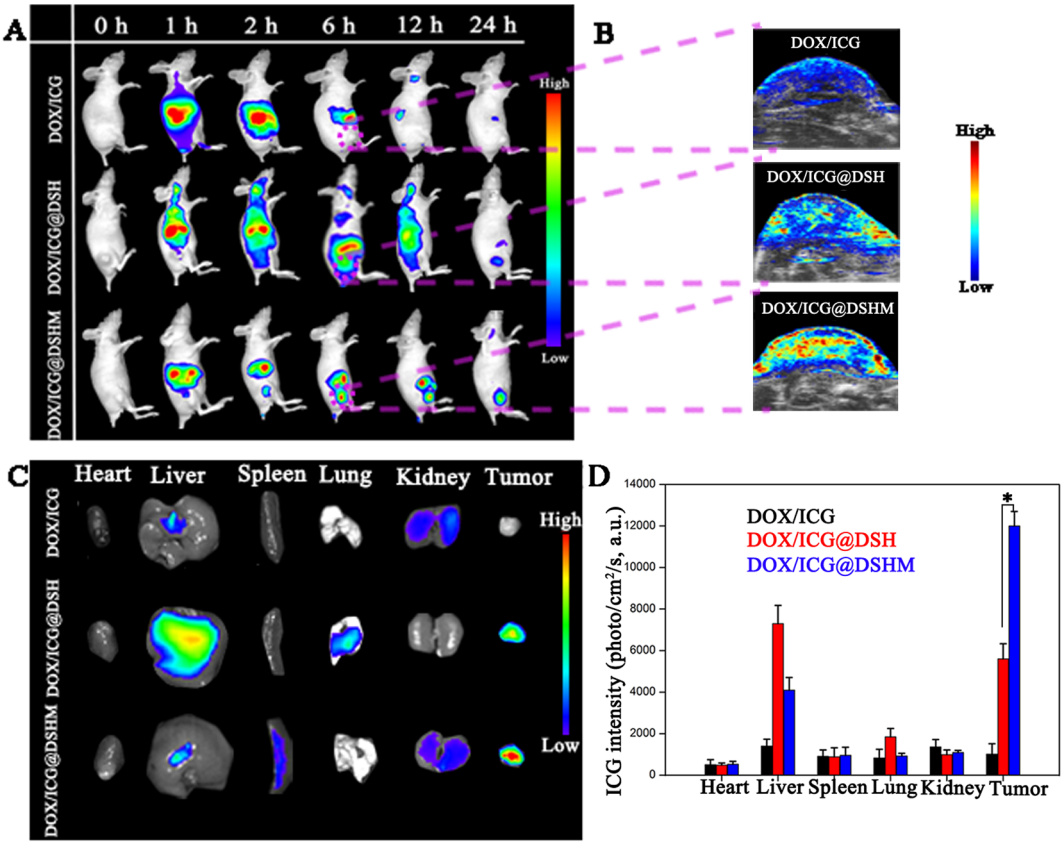

Fig. 6. (A) In vivo NIR fluorescence imaging of MCF-7 tumor-bearing nude mice at 1, 2, 6, 12, and 24 h post-*i.v.* injection of DOX/ICG, DOX/ICG@DSH, and DOX/ICG@DSHM. (B) In vivo PA imaging of MCF-7 tumor-bearing nude mice at 6 h post-*i.v.* injection of DOX/ICG, DOX/ICG@DSH, and DOX/ICG@DSHM. (C) *Ex vivo* NIR fluorescence imaging and (D) average NIR fluorescence intensity of tumors/major organs of MCF-7 tumor-bearing nude mice at 6 h post-*i.v.* injection of DOX/ICG, DOX/ICG@DSH, and DOX/ICG@DSHM.

vitro cytotoxicity of the DOX/ICG@DSHM-treated group was also much more effective in comparison with that of DOX/ICG@DCHM-treated group (Fig. S6). Furthermore, combined with the result of *in vitro* drug release and cytotoxicity, the reduction-responsive DOX/ICG@DSHM with excellent performances were investigated in the following studies.

2.8. In vivo fluorescence/PA imaging

The biodistribution of the DOX/ICG@DSHM were employed to determine the tumor-targeting capability using noninvasive NIR imaging technique. Different formulations including DOX/ICG, DOX/ICG@DSH, and DOX/ICG@DSHM were administrated into the MCF-7 tumor-bearing nude mice by intravenous injection respectively. Fluorescence signals of the DOX/ICG, DOX/ICG@DSH, and DOX/ICG@DSHM-treated mice were distributed in the whole body at1 h after intravenous injection (Fig. 6A). Then, strong fluorescence signals of the dual-targeting DOX/ICG@DSHM could be observed in the tumor at 6 h after intravenous injection. Moreover, the fluorescence signals from tumor are gradually increased and these fluorescence signals could be detected even at 24 h. In contrast, weaker fluorescence/PA signals of the free DOX/ICG and single-targeting DOX/ICG@DSH-treated group were detected at the tumor sites (Fig. 6A and B). The results revealed the important role of HA and MTX in promoting the efficient tumor accumulation of DOX/ICG@DSHM at the tumor sites via dual-active targeting mechanisms. Besides, the result also implied the prolonged blood circulation of DOX/ICG@DSH and DOX/ICG@DSHM.

In addition, after 24 h post-injection, the mice were immediately euthanized, and then the tumors and normal organs were excised for *ex*

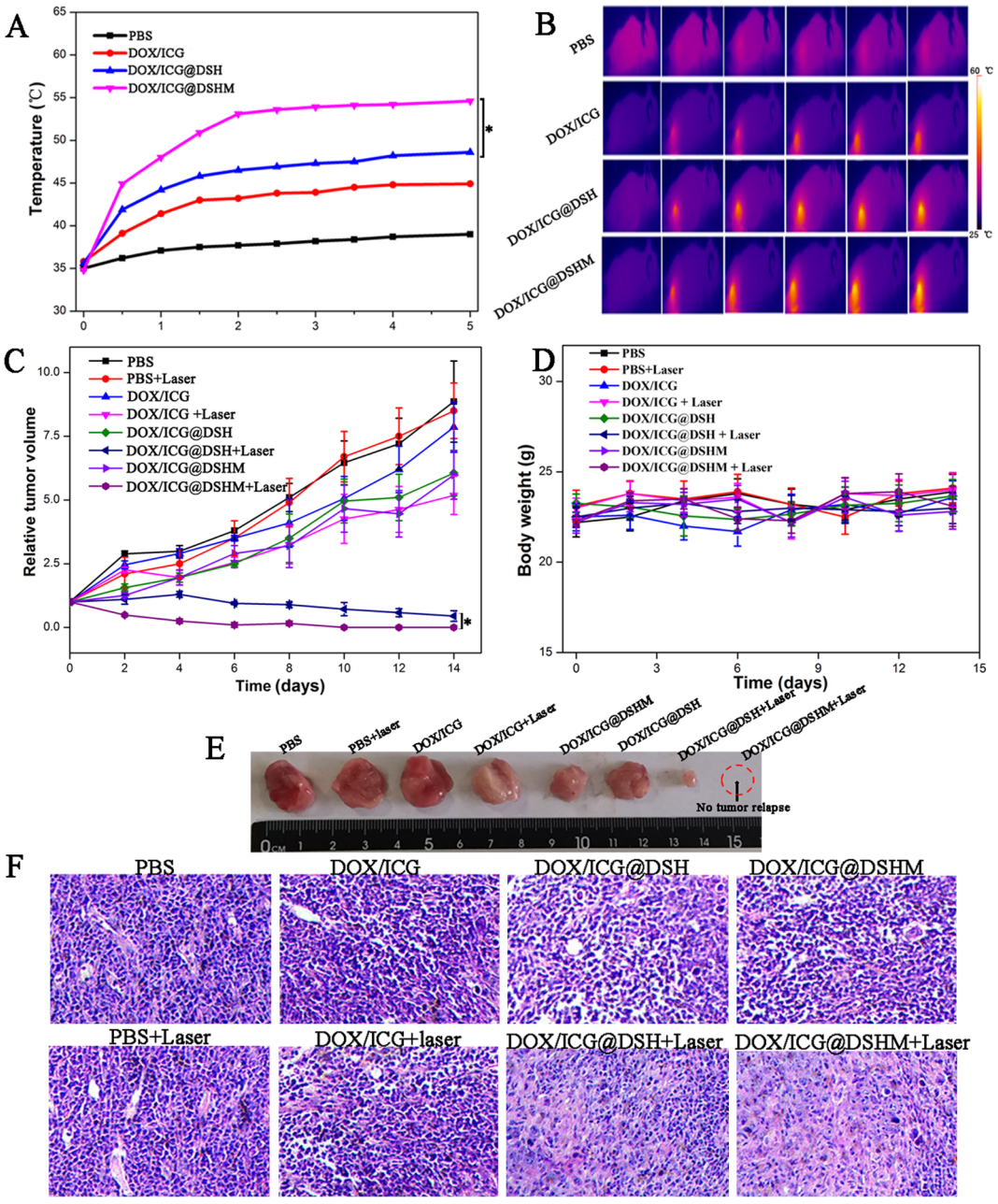

Fig. 7. (A) Time-dependent tumor temperature increase and (B) infrared thermal images of MCF-7 tumor-bearing nude mice irradiated by 808-nm laser (1 W/cm^2) at 6 h after intravenous injection of PBS, free DOX/ICG, DOX/ICG@DSH, and DOX/ICG@DSHM. (C) Relative tumor volume and (D) body weight changes of MCF-7 tumor-bearing nude mice during the treatment. (E) Representative photographs of the excised tumors at the end of the treatment. (F) H&E staining of the excised tumors.

vivo fluorescence imaging (Fig. 6C and D). Superior fluorescence signals were also observed in the tumors of the DOX/ICG@DSHM-treated group compared to those of DOX/ICG@DSH and free DOX/ICG-treated group, confirming the efficient accumulation of dual-active targeting nanosystems at the tumor sites. Besides, it was undeniable that the relatively strong fluorescence of both DOX/ICG@DSHM and DOX/ICG@DSH-treated groups could be also observed in the liver, resulting from the non-specific uptake by reticulo-eneothelial system (RES). Notably, the average fluorescence intensity of DOX/ICG@DSHM in the tumors was 2.5-fold than that of DOX/ICG@DSH. Overall, these results decisively validated excellent specific tumor dual-targeting of DOX/ICG@DSHM, which could be attributed to the advantages of EPR effect-mediated passive targeting combined with active targeting cellular uptake.

2.9. *In vivo* photothermal effect and chemo-photothermal efficiency

Encouraged by the above *in vitro* and *in vivo* results, the investigation of synergistic chemo-photothermal therapy mediated by DOX/ICG@DSH and DOX/ICG@DSHM were further conducted on BALB/C nude mice. The mice were injected intravenously with PBS, DOX/ICG, DOX/ICG@DSH, and DOX/ICG@DSHM respectively.

Firstly, the photothermal imaging was recorded using infrared imaging camera after 5 min laser irradiation (808 nm, 1 W/cm^2, 5 min). After 808 nm irradiation for 5 min, the temperatures in the PBS-treated negative control groups and free DOX/ICG-treated positive control groups displayed negligible temperature changes, which was ineffective to damage tumor tissues (temperature above 42–47 °C was reported to induce the selective destruction of the tumor cells) [29]. In contrast, the tumor surface temperature could rapidly rise to 47.7 °C and 52.6 °C after injecting with DOX/ICG@DSH and DOX/ICG@DSHM, respectively, which could create irreversible tumor tissue damage (Fig. 7A and B). More importantly, the DOX/ICG@DSHM induced a higher temperature in the tumor areas than that of DOX/ICG@DSH, implying the superiority of folate/CD_{44} receptor-mediated cellular uptake and internalization with the help of EPR effect-mediated passive tumor targeting.

To monitor the tumor growth, the tumor volumes were also recorded (Fig. 7C). Rapid growth occurred in PBS or PBS plus laser groups, indicating that the 808 nm laser irradiation alone had a negligent effect on the tumor growth. Additionally, the tumor volume of the free DOX/ICG-treated group also grew rapidly after exposing to the laser or not, which indicated that the tumor growth could not be inhibited effectively by single injection of DOX/ICG at low dose. These

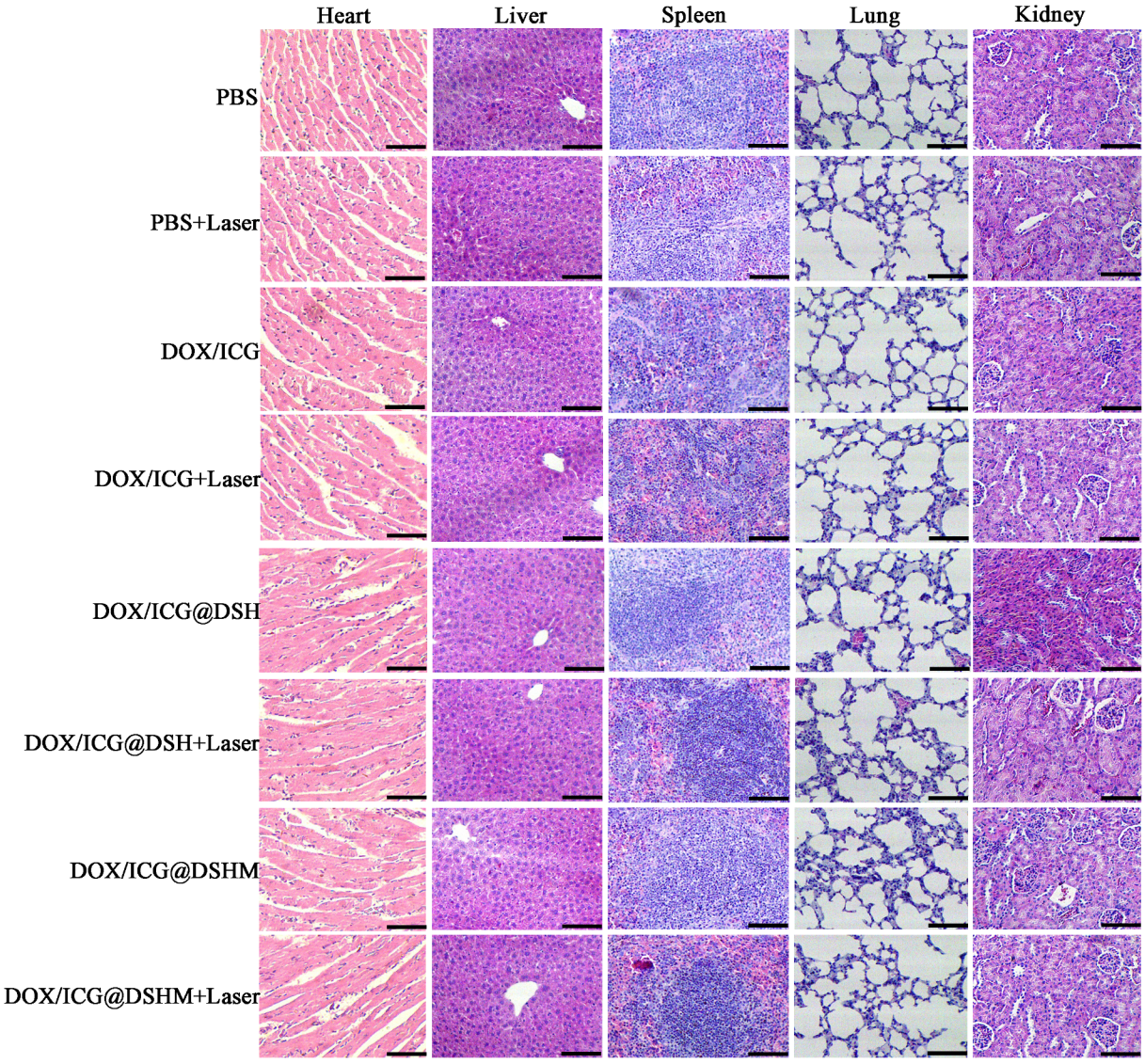

Fig. 8. H&E staining of primary organs of MCF-7 tumor-bearing mice treated with DOX/ICG, DOX/ICG@DSH, and DOX/ICG@DSHM with or without 808-nm NIR irradiation. Scale bars = 300 μm.

were resulted from the insufficient concentration enrichment of DOX and ICG in tumors, which was a universal biomedical phenomenon caused by poor pharmacokinetics of small molecular drug. Besides, in the DOX/ICG@DSHM and DOX/ICG@DSH-treated groups without NIR laser irradiation, the tumor growth was slightly inhibited, which was attributed to the higher accumulation of DOX/ICG@DSHM and DOX/ICG@DSH in tumors than that of free DOX/ICG. Notably, by treating with DOX/ICG@DSHM and DOX/ICG@DSH under NIR lase irradiation, the tumor growth on mice was greatly inhibited due to the combination of the chemo-photothermal treatment. More importantly, the tumor of mice treated with DOX/ICG@DSHM plus laser irradiation was completely ablated without tumor recurrence (Fig. 7E). This result not only indicated that the excellent synergistic therapy was very important but also confirmed that the dual targeted delivery strategy of DOX/ICG@DSHM could enhance the intracellular accumulation of DOX/ICG, resulting in a more pronounced chemotherapeutic and photothermal cytotoxicity. Additionally, the reduction-responsive drug delivery system also avoided the unwanted leakage of DOX/ICG in the blood circulation, which could guarantee the effective enrichment of both chemotherapeutic drug and photothermal agent in tumor. Moreover, the antitumor effect was also investigated using H&E staining. As shown in Fig. 7F, the DOX/ICG@DSHM-treated group plus laser irradiation displayed the superior cell-killing effect with widespread apoptosis and necrosis of cancer cells.

Furthermore, the body weights of the mice in each group, an indicator of the treatment-induced toxicity [30], were also monitored. As shown in Fig. 7D, there was no significant variation in the DOX/ICG@DSHM-treated group plus laser irradiation, implying that there was no acute side effect in this combination therapy. In addition, the histology analysis of H&E-stained major organs of the DOX/ICG@DSHM-treated group plus laser irradiation proved no obvious sign of organ damage or other abnormality (Fig. 8).

3. Conclusion

In summary, we synthesized a novel dual-targeting reduction-responsive DOX/ICG@DSHM by the co-encapsulation of DOX/ICG using DA-SS-HA-MTX, which combined both synergistic active targeting ability and chemo-photothermal therapy for cancer treatment. DOX/ICG@DSHM possessed on-demand release ability of DOX and remarkably enhanced the photo-stability of ICG. The dual-targeting DOX/ICG@DSHM could effectively promote the cellular uptake of DOX/ICG via folate/CD_{44} receptor-mediated endocytosis. In addition, the DOX/ICG@DSHM could realize an efficient tumor accumulation with prolonged blood circulation, which was confirmed by *in vivo* NIR fluorescence and PA imaging. Notably, under laser irradiation, this multimodal therapy not only greatly induced cancer cell death *in vitro*, but also significantly suppressed tumor growth *in vivo*. Hence, the dual-targeting reduction-responsive DOX/ICG@DSHM with NIR laser irradiation would be a promising strategy for enhancing chemo-photothermal anticancer therapy.

Declaration of Competing Interest

The authors declare that they have no known competing financial interests or personal relationships that could have appeared to influence the work reported in this paper.

Acknowledgements

This work was support by grants from the the National Key R&D Program of China (2018YFA0108304), the National Natural Science Foundation of China (81771271), and the Fujian Provincial Health Education Joint Research Project (WKJ2016-2-20).

Appendix A. Supplementary data

Supplementary data to this article can be found online at https://doi.org/10.1016/j.cej.2019.122426.

References

[1] T. Ramasamy, H.B. Ruttala, B. Gupta, B.K. Poudel, H.G. Choi, C.S. Yong, J.O. Kim, Smart chemistry-based nanosized drug delivery systems for systemic applications: a comprehensive review, J. Controlled Release 258 (2017) 226–253.
[2] H. Maeda, Toward a full understanding of the EPR effect in primary and metastatic tumors as well as issues related to its heterogeneity, Adv. Drug Deliv. Rev. 91 (2015) 3–6.
[3] W. Wang, G. Liang, W. Zhang, D. Xing, X. Hu, Cascade-promoted photo-chemotherapy against resistant cancers by enzyme-responsive polyprodrug nanoplatforms, Chem. Mater. 30 (10) (2018) 3486–3498.
[4] S. Guan, Y. Weng, M. Li, R. Liang, C. Sun, X. Qu, S. Zhou, An NIR-sensitive layered supramolecular nanovehicle for combined dual-modal imaging and synergistic therapy, Nanoscale 9 (29) (2017) 10367–10374.
[5] M. Zheng, C. Yue, Y. Ma, P. Gong, P. Zhao, C. Zheng, Z. Sheng, P. Zhang, Z. Wang, L. Cai, Single-step assembly of DOX/ICG loaded lipid–polymer nanoparticles for highly effective chemo-photothermal combination therapy, ACS Nano 7 (3) (2013) 2056–2067.
[6] Y. Li, J. Lin, J. Ma, L. Song, H. Lin, B. Tang, D. Chen, G. Su, S. Ye, X. Zhu, F. Luo, Z. Hou, Methotrexate-camptothecin prodrug nanoassemblies as a versatile nanoplatform for biomodal imaging-guided self-active targeted and synergistic chemotherapy, ACS Appl. Mater. Interfaces 9 (40) (2017) 34650–34665.
[7] Y. Li, G. Liu, J. Ma, J. Lin, H. Lin, G. Su, D. Chen, S. Ye, X. Chen, X. Zhu, Z. Hou, Chemotherapeutic drug-photothermal agent co-self-assembling nanoparticles for near-infrared fluorescence and photoacoustic dual-modal imaging-guided chemo-photothermal synergistic therapy, J. Controlled Release 258 (2017) 95–107.
[8] S. Tenzer, D. Docter, J. Kuharev, A. Musyanovych, V. Fetz, R. Hecht, F. Schlenk, D. Fischer, K. Kiouptsi, C. Reinhardt, K. Landfester, H. Schild, M. Maskos, S.K. Knauer, R.H. Stauber, Rapid formation of plasma protein corona critically affects nanoparticle pathophysiology, Nat. Nanotechnol. 8 (10) (2013) 772–781.
[9] M. Zheng, P. Zhao, Z. Luo, P. Gong, C. Zheng, P. Zhang, C. Yue, D. Gao, Y. Ma, L. Cai, Robust ICG theranostic nanoparticles for folate targeted cancer imaging and highly effective photothermal therapy, ACS Appl. Mater. Interfaces 6 (9) (2014) 6709–6716.
[10] W. Zhang, X. Hu, Q. Shen, D. Xing, Mitochondria-specific drug release and reactive oxygen species burst induced by polyprodrug nanoreactors can enhance chemotherapy, Nat. Commun. 10 (1) (2019) 1704.
[11] J.Y. Lee, U. Termsarasab, J.H. Park, S.Y. Lee, S.H. Ko, J.S. Shim, S.J. Chung, H.J. Cho, D.D. Kim, Dual CD44 and folate receptor-targeted nanoparticles for cancer diagnosis and anticancer drug delivery, J. Controlled Release 236 (2016) 38–46.
[12] J. Miller-Kleinhenz, X. Guo, W. Qian, H. Zhou, E.N. Bozeman, L. Zhu, X. Ji, Y.A. Wang, T. Styblo, R. O'Regan, H. Mao, L. Yang, Dual-targeting Wnt and uPA receptors using peptide conjugated ultra-small nanoparticle drug carriers inhibited cancer stem-cell phenotype in chemo-resistant breast cancer, Biomaterials 152 (2018) 47–62.
[13] J.M. Rosenholm, E. Peuhu, L.T. Bate-Eya, J.E. Eriksson, C. Sahlgren, M. Linden, Cancer-cell-specific induction of apoptosis using mesoporous silica nanoparticles as drug-delivery vectors, Small 6 (11) (2010) 1234–1241.
[14] K. Mizusawa, Y. Takaoka, I. Hamachi, Specific cell surface protein imaging by extended self-assembling fluorescent turn-on nanoprobes, J. Am. Chem. Soc. 134 (32) (2012) 13386–13395.
[15] J. Chen, L. Huang, H. Lai, C. Lu, M. Fang, Q. Zhang, X. Luo, Methotrexate-loaded PEGylated chitosan nanoparticles: synthesis, characterization, and in vitro and in vivo antitumoral activity, Mol. Pharm. 11 (7) (2014) 2213–2223.
[16] Z. Chen, N. He, M. Chen, L. Zhao, X. Li, Tunable conjugation densities of camptothecin on hyaluronic acid for tumor targeting and reduction-triggered release, Acta Biomater. 43 (2016) 195–207.
[17] Y. Li, L. Song, J. Lin, J. Ma, Z. Pan, Y. Zhang, G. Su, S. Ye, F.H. Luo, X. Zhu, Z. Hou, Programmed nanococktail based on ph-responsive function switch for self-synergistic tumor-targeting therapy, ACS Appl. Mater. Interfaces 9 (45) (2017) 39127–39142.
[18] X. Hu, S. Zhai, G. Liu, D. Xing, H. Liang, S. Liu, Concurrent drug unplugging and permeabilization of polyprodrug-gated crosslinked vesicles for cancer combination chemotherapy, Adv. Mater. 30 (21) (2018) e1706307.
[19] A. Zhu, K. Miao, Y. Deng, H. Ke, H. He, T. Yang, M. Guo, Y. Li, Z. Guo, Y. Wang, X. Yang, Y. Zhao, H. Chen, Dually pH/reduction-responsive vesicles for ultrahigh-contrast fluorescence imaging and thermo-chemotherapy-synergized tumor ablation, ACS Nano 9 (8) (2015) 7874–7885.
[20] S. Yin, J. Huai, X. Chen, Y. Yang, X. Zhang, Y. Gan, G. Wang, X. Gu, J. Li, Intracellular delivery and antitumor effects of a redox-responsive polymeric paclitaxel conjugate based on hyaluronic acid, Acta Biomater. 26 (2015) 274–285.
[21] X. Hu, G. Liu, Y. Li, X. Wang, S. Liu, Cell-penetrating hyperbranched polyprodrug amphiphiles for synergistic reductive milieu-triggered drug release and enhanced magnetic resonance signals, J. Am. Chem. Soc. 137 (1) (2015) 362–368.
[22] X. Hu, J. Hu, J. Tian, Z. Ge, G. Zhang, K. Luo, S. Liu, Polyprodrug amphiphiles: hierarchical assemblies for shape-regulated cellular internalization, trafficking, and drug delivery, J. Am. Chem. Soc. 135 (46) (2013) 17617–17629.
[23] H. Zhang, W. Li, X. Guo, F. Kong, Z. Wang, C. Zhu, L. Luo, Q. Li, J. Yang, Y. Du,

J. You, Specifically increased paclitaxel release in tumor and synergetic therapy by a hyaluronic acid-tocopherol nanomicelle, ACS Appl. Mater. Interfaces 9 (24) (2017) 20385–20398.
[24] C. Abels, S. Fickweiler, P. Weiderer, W. Baumler, F. Hofstadter, M. Landthaler, R.M. Szeimies, Indocyanine green (ICG) and laser irradiation induce photooxidation, Arch. Dermatol. Res. 292 (8) (2000) 404–411.
[25] C. Feng, M. Rui, H. Shen, Y. Xin, J. Zhang, J. Li, L. Yue, W. Lai, X. Xu, Tumor-specific delivery of doxorubicin through conjugation of pH-responsive peptide for overcoming drug resistance in cancer, Int. J. Pharm. 528 (1–2) (2017) 322–333.
[26] Y. Chi, X. Yin, K. Sun, S. Feng, J. Liu, D. Chen, C. Guo, Z. Wu, Redox-sensitive and hyaluronic acid functionalized liposomes for cytoplasmic drug delivery to osteosarcoma in animal models, J. Control. Release 261 (2017) 113–125.
[27] J. Yang, H. Su, W. Sun, J. Cai, S. Liu, Y. Chai, C. Zhang, Dual Chemodrug-loaded single-walled carbon nanohorns for multimodal imaging-guided chemo-photothermal therapy of tumors and lung metastases, Theranostics 8 (7) (2018) 1966–1984.
[28] M. Hu, P. Huang, Y. Wang, Y. Su, L. Zhou, X. Zhu, D. Yan, Synergistic combination chemotherapy of camptothecin and floxuridine through self-assembly of amphiphilic drug-drug conjugate, Bioconjug. Chem. 26 (12) (2015) 2497–2506.
[29] F. Yan, W. Duan, Y. Li, H. Wu, Y. Zhou, M. Pan, H. Liu, X. Liu, H. Zheng, NIR-laser-controlled drug release from DOX/IR-780-loaded temperature-sensitive-liposomes for chemo-photothermal synergistic tumor therapy, Theranostics 6 (13) (2016) 2337–2351.
[30] P. Zhao, M. Zheng, C. Yue, Z. Luo, P. Gong, G. Gao, Z. Sheng, C. Zheng, L. Cai, Improving drug accumulation and photothermal efficacy in tumor depending on size of ICG loaded lipid-polymer nanoparticles, Biomaterials 35 (23) (2014) 6037–6046.